Order-disorder type of Peierls instability in $BaVS_3$

Vita Ilakovac,[1,2,*] Adrien Girard,[3,†] Victor Balédent,[4,‡] Pascale Foury-Leylekian,[4,§] Bjoern Winkler,[5,‖] Ivan Kupčić,[6,¶]
Helmuth Berger,[7,#] Alexeï Bosak,[8,**] and Jean-Paul Pouget[4,††]
[1]*Sorbonne Université, CNRS, Laboratoire de Chimie Physique—Matière et Rayonnement, F-75252 Paris, France*
[2]*Département de Physique, CY Cergy Paris Université, F-95031 Cergy-Pontoise, France*
[3]*Sorbonne Université, CNRS, MONARIS, F-75252 Paris, France*
[4]*Université Paris-Saclay, CNRS, Laboratoire de Physique des Solides, 91405, Orsay, France*
[5]*Institut für Geowissenschaften, Goethe Universität Frankfurt, D-60438 Frankfurt am Main, Germany*
[6]*Department of Physics, Faculty of Science, University of Zagreb, HR-10002 Zagreb, Croatia*
[7]*Ecole Polytechnique Fédérale de Lausanne (EPFL), CH-1015 Lausanne, Switzerland*
[8]*ESRF—The European Synchrotron, 71, F-38000 Grenoble, France*

(Received 27 August 2020; accepted 24 December 2020; published 14 January 2021)

Lattice dynamics of low-dimensional $BaVS_3$ is reported across the metal-insulator Peierls transition occurring at $T_P = 69$ K using a combination of the thermal diffuse scattering of x rays, inelastic x-ray scattering, and density-functional theory calculations. The nondetection of a Kohn anomaly points to a unique situation of an order-disorder Peierls instability with a quasielastic critical scattering which has been fully characterized. These observations are discussed in the scope of a Peierls instability dominated by strong electron-phonon coupling and/or nonadiabatic effects.

DOI: 10.1103/PhysRevB.103.014306

I. INTRODUCTION

The mechanism of the q-momentum anomaly in the frequency dependence of low-frequency phonon branches is established in metals since the pioneering calculation of W. Kohn [1] and its first detection in Pb [2] in the 1960s. But it is only with *ab initio* calculations of the phonon spectrum including the electron-phonon coupling that such anomalies could be predicted in more complex systems [3]. In the adiabatic approximation the so-called Kohn anomaly in the phonon spectrum is due to an efficient screening of ion-ion interaction by the conduction electrons which is related to the shape of the Fermi surface [4]. More precisely in the weak electron-phonon coupling limit, the Kohn anomaly in the phonon spectrum directly reflects the singular q-dependent part of the electron-hole or Lindhard response of the electron gas. This singularity is enhanced when the spatial dimension of the electron gas is reduced [4]. Thus for a one-dimensional (1D) conductor undergoing a Peierls instability one expects, in the adiabatic approximation and in the perturbative treatment of the electron-phonon coupling, the formation of a giant Kohn anomaly at the $2k_F$ wave vector (k_F being the Fermi momentum of the 1D electron gas) [5]. Indeed a sharp $2k_F$ Kohn anomaly has been observed in the Krogmann salt $K_2Pt(CN)_4Br_{0.3} \cdot 3H_2O$ [6] and in the blue bronze $K_{0.3}MoO_3$ [7]. In the latter compound it has been consistently shown that experiments follow quite well the expectations of the weak-coupling scenario of the Peierls transition which leads to a displacive type of lattice instability [8]. However, the formation of a pronounced $2k_F$ Kohn anomaly is not the general rule for 1D conductors (for a recent review see Ref. [9]). For example the organic conductor TTF-TCNQ exhibits only a weak and broad Kohn anomaly, whose frequency does not soften significantly on approaching the Peierls transition [10]. A somewhat similar situation was reported in 2D metals such as the transition metal dichalcogenide 2H $NbSe_2$ where an earlier neutron scattering investigation revealed the formation of a broad Kohn anomaly accompanied by a zero-energy critical scattering which reflects a pronounced order-disorder type of lattice instability [11]. However, a recent high-resolution inelastic x-ray scattering (IXS) investigation of 2H $NbSe_2$ shows that the Peierls phonon mode exhibits in fact both a critical frequency softening and damping enhancement on approaching the Peierls transition [12]. This mixed displacive/order-disorder character of the Peierls transition dynamics is beyond the classical weak-coupling–adiabatic scenario. Thus new scenarios which have been proposed rely on q-dependent electron-phonon coupling [13], strong electron-phonon coupling [9,14,15], or nonadiabaticity. The first type of scenario achieves, through anharmonic effects induced by the coupling to electrons, a broad Kohn anomaly, while the second and third types of scenario favor an order-disorder type of critical dynamics. However, these

---

[*] vita.ilakovac-casses@sorbonne-universite.fr
[†] adrien.girard@sorbonne-universite.fr
[‡] victor.baledent@universite-paris-saclay.fr
[§] pascale.foury@universite-paris-saclay.fr
[‖] b.winkler@kristall.uni-frankfurt.de
[¶] ivan.kupcic@phy.hr
[#] helmuth.berger@epfl.ch
[**] alexsei.bossak@esrf.fr
[††] jean-paul.pouget@u-psud.fr

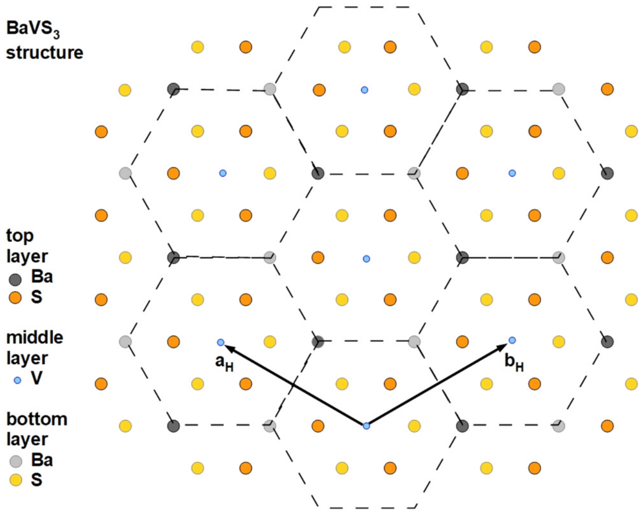

FIG. 1. Room-temperature hexagonal structure of $BaVS_3$, seen along the c axis, presenting a top BaS_3 plane, a middle V layer, and a bottom BaS_3 layer. a_H, b_H are for the hexagonal unit cell wave vectors. According to recent structural refinements [16] the Ba/S and V subsystems are not adjusted in terms of space group at RT.

scenarios do not entirely explain the observed Peierls dynamics of the transition metal dichalcogenides. Here we report the first unambiguous observation of an order-disorder type of dynamics in the Peierls compound $BaVS_3$.

The room-temperature (RT) structure of this $3d^1$ transition metal compound is shown in Fig. 1. It consists of a hexagonal packing of quasi-1D chains of face-sharing VS_6 octahedra directed along the c axis, separated by Ba atoms [17]. Its structural anisotropy suggests properties of a linear chain compound but with a rather low conductivity anisotropy ratio $\sigma_c/\sigma_a \approx 3$ [18]. A zigzag deformation of the V chains at $T_S = 250$ K reduces the crystal symmetry from hexagonal to orthorhombic [19], without significant changes in the resistivity and the paramagnetic properties [18]. A semiconducting behavior is observed below the temperature of the resistivity minimum, $T_m \approx 130$ K, [17,18,20] and an extra feature shows up in the pre-edge of the V L-edge linear dichroism [21]. This suggests additional electronic transformations which are not yet clearly elucidated but which could be associated with a host-guest space-group adjustment of Ba/S and V sublattices [16]. At $T_P = 69$ K the system undergoes a metal-to-insulator (MI) transition, accompanied by a doubling of the unit cell in the c direction [22]. The driving force of the MI transition is the Peierls instability resulting in the formation of charge density waves (CDWs) along the V-S chains [23]. Spin degrees of freedom are affected at T_P [18], but an incommensurate antiferromagnetic order establishes only below $T_N = 30$ K [24–27].

Local density approximation (LDA) calculations reveal a peculiar interplay between two different types of active electrons at the Fermi level: two narrow E_g bands (localized states) and one dispersive (itinerant states), with a mainly A_{1g} character, extending along the c^* direction [28–30]. But the LDA A_{1g} band is found to be almost complete. This is incompatible with the experimental results pointing to an equipartitial A_{1g}/E_g occupation [23]. The discrepancy is corrected when considerable correlation/exchange effects are included through dynamic mean-field theory [31–33].

The Peierls transition achieves also an ordering between the A_{1g} and E_g orbitals [32,34,35]. In the Peierls ground state occurring below T_P, A_{1g} electrons are paired into magnetic singlets while E_g electrons keep their spin free. The E_g spins order antiferromagnetically (AF) at T_N [25,27]. Under pressure T_P drastically drops [36,37], while T_N stays constant [38]. At 1.4 GPa T_P and T_N merge together and the q_P modulation of the Peierls state becomes incommensurate, while at 1.8 GPa the two ground states conjointly vanish [36–38]. The drastic drop of T_P has been ascribed to a decrease of the lifetime of the A_{1g} electron-hole pairs due to their hybridization with the nonpaired E_g orbitals [27]. Furthermore, a quantitative analysis of the drop of T_P under pressure suggests that the Peierls transition of $BaVS_3$ could occur in the nonadiabatic (antiadiabatic) limit [27,37]. Note that in this limit the dynamics of the Peierls chain calculated for free electrons and for a weak electron-phonon coupling is of the order-disorder type [9].

Recent combined thermal diffuse scattering (TDS) and IXS investigation of the $BaVS_3$ lattice dynamics across T_S shows that the orthorhombic distortion is triggered by the softening of a Γ phonon [39]. In this work, we present an equivalent study of the metal-insulator Peierls transition. We first present diffuse scattering (DS) data in the $l = 1/2$ plane and corresponding model calculation in order to identify the major phonon contribution. Further, IXS results show that the low-energy phonons are optical in nature and that they do not soften. The analysis of the q width of the DS related to the q_P wave vector gives the insight in the evolution of the spatial extension of the fluctuating domains while the energy width of the IXS central peak points to their life-time evolution. All these results point to an original situation where the structural transition at T_S is displacive and phonon driven, while the Peierls transition at T_P is of order-disorder type. This unique results is discussed in terms of the models including strong electron-phonon coupling and nonadiabaticity.

II. EXPERIMENT

Single crystals of $BaVS_3$, of a needlelike shape along the [001] axis, were grown by the tellurium flux method [40]. They were slightly polished to obtain lateral dimensions of about 100 μm in order to maximize the IXS signal and then mounted on a glass fiber and fixed with an epoxy glue. x-ray DS experiments were conducted first with the diffractometer built as a side station at the ID28 beamline [41] of the European Synchrotron Radiation Facility (ESRF), with a monochromatic beam of 17.8-keV photons. The DS maps were recorded with a Pilatus 3 X 1M detector in the range 30–300 K. Closed-cycle cryocooler with Kapton windows was used for both IXS and DS measurement. In the case of DS data collection, an internal screen was added, which was rotating in opposite direction relatively to the cryostat movement. It allowed us to suppress the background scattering from both entrance and exit windows. The IXS experiments were conducted at the ID28 beamline of the ESRF, with the high-resolution spectrometer operating at an energy of 17.8

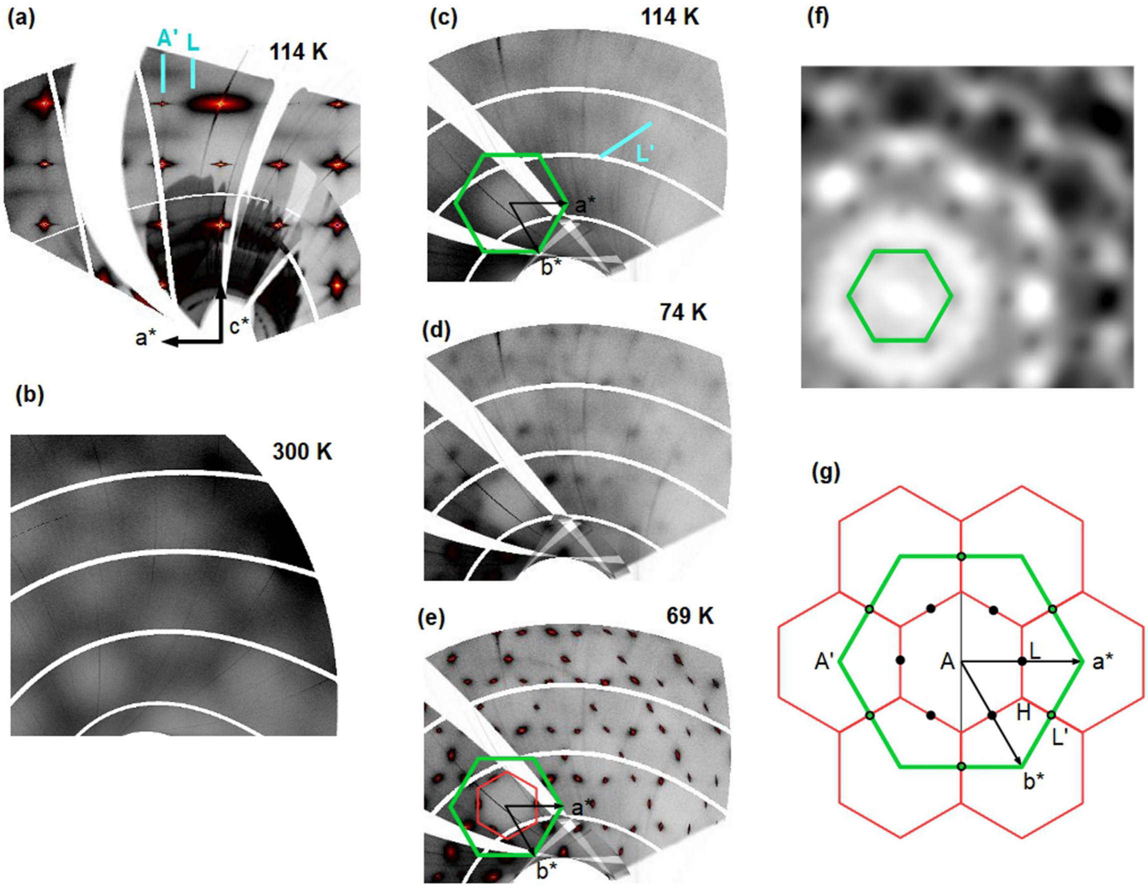

FIG. 2. Reconstruction of the $(h, 0, l)$ plane at 114 K (a), and the $(h, k, 3.5)$ plane at 300 K (b), 114 K (c), 74 K (d), and 69 K (e). Calculated TDS intensity, including only inelastic contribution and corresponding to the Cmc2_1 space group is shown in (f). It should be compared to the diffuse scattering (DS) map in (c). The first Brillouin zone (BZ), six shifted first BZ covering a part of the second BZ (red lines), and a diffuse hexagon (green line) are schematically shown in (g). High-symmetry points A, H, L, are indicated in the first BZ. A′ and L′ are the equivalent points out of the first BZ. Black full (open) circles show the positions of the satellites in the first (shifted first) BZ, which are L (L′) points, respectively. The first BZ and a diffuse hexagon are shown in (e), while solely a diffuse hexagon position is given in (c) and (f). Light blue lines in (a) and (c) indicate line scans in DS maps. Points A′ (diffuse hexagon corner) and L are scanned in the c^* direction in (a), while L′ is scanned in the $a^* + b^*$ direction in (c). The analysis of the scans is presented in Fig. 4. Unit cell wave vectors are given in hexagonal settings.

keV. With our setup, the energy resolution was about 3 meV. A correction of 10 K (14 K) is applied in IXS (DS) scans in order to match the temperature of the structural transition with the MI transition determined by conductivity measurements, 69 K [18]. Scattering angle restrictions imposed the choice of representative DS reconstruction as $(h, k, 3.5)$. However, different mount allowed us to explore essentially equivalent $(h, k, 4.5)$ plane by IXS, thus gaining the intensity. CrysAlis software (Rigaku–Oxford Diffraction) was used for the preliminary diffraction data reconstructions. High-quality reconstructions were performed with locally developed software.

III. RESULTS

A. Diffuse scattering

1. DS maps

The reconstruction of the $(h, 0, l)$ plane of BaVS$_3$, measured at 114 K is shown Fig. 2(a). At $l = n + 1/2$, it shows diffuse streaks extending in a^* direction. They correspond to a hexagonal, honeycomb-shaped diffusion, visible already at RT in the reconstruction of the $(h, k, 3.5)$ plane [see Fig. 2(b)]. At low temperature, when approaching T_P from above, it disappears and is replaced by a diffuse-scattering spot-pattern which condenses in superstructure satellites at T_P, see Figs. 2(c)–2(e). Note that the intensity range of the DS taken at low temperature is modified relatively to this at 300 K, in order to make the diffusion pattern more visible. The corresponding figures presented in the same intensity range are shown in the Appendix (see Fig. 11). The intensity of the honeycomb-shaped diffusion, as measured at the A′ point (diffuse hexagon corner), underlines all important changes in BaVS$_3$, see Fig. 3. When lowering the temperature, it increases at the orthorhombic transition (T_S), strongly decreases at the minimum of resistivity (T_m) and progressively vanishes below the Peierls transition (T_P).

The reduced wave vector of the superstructure satellites [see Fig. 2(e)] appearing at T_P is (0.5, 0, 0.5) in hexagonal settings (space group P6$_3$/mmc), which will be used throughout this work. This correspond to the point L of the first Brillouin zone (BZ), as shown by black points in Fig. 2(g). Other satellites are equivalent due to the symmetry operations

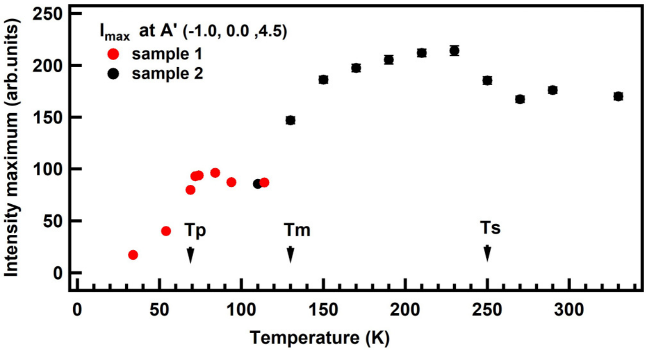

FIG. 3. Temperature dependence of the DS intensity at the A′ point. It is derived from two distinct measurements, performed on two different samples. Sample 1 (red points) is a pure BaVS$_3$, studied in this work. Black points are revisited data from a slightly Al-doped sample, studied previously [39]. The intensity of the second measurements is normalized in order to obtain the same intensity at a common temperature of about 110 K.

of the P6$_3$/mmc space group. One third of them are located at the diffuse hexagon edge, and are indicated by open circles in Fig. 2(g) (L′ points). As the honeycomb-shaped diffusion exceeds the first BZ, the behavior of the satellites at the L and L′ points are compared throughout the presented work. Remark that in orthorhombic settings (space group Cmc2$_1$), and for a single-twin domain, the satellite is at the reduced wave vector (1, 0, 0.5) [16,22,23].

Hexagon-shaped diffusion is observed in (h, k, 3.5) and (h, k, 4.5) planes. But it is not visible in the (h, k, 2.5) plane (not shown), where only diffuse spots appear at satellites positions above T_P. The increase of the hexagonal DS intensity with l shows that the scattering is of displacive nature, with a predominantly c (z) direction of atomic displacement. In order to understand the origin of the diffuse hexagons, we performed lattice dynamics calculation within density-functional theory (DFT) implemented in the CASTEP code [42,43] and following the formalism detailed in Ref. [44]. TDS-map calculation of the (h, k, 3.5) plane in the Cmc2$_1$ space group is shown Fig. 2(f). The analysis is presented in detail in the Appendix. The calculation shows that the TDS is a result of phonons of an energy of about 6–9 meV, due mostly to an out of phase motion in the z direction of the two Ba ions in the unit cell.

2. Momentum-space temperature evolution

In order to determine the temperature evolution of the spatial extension of the pretransitional fluctuations above T_P, we have measured the profile of the diffuse scattering. This was done at two positions where a satellite appears below T_P, and for the position of a diffuse hexagon corner. The satellite L (−0.5, 0, −4.5) and the diffuse hexagon corner A′ (−1.0, 0, −4.5) were scanned along the c^* direction, as shown by light blue lines in Fig. 2(a). The second satellite, L′ (3, −1.5, 3.5) was scanned in $a^* + b^*$ direction (perpendicular to c^*), as shown in Fig. 2(c).

The data analysis of the profiles was performed using a Lorentzian function deconvoluted by the experimental resolution. Assuming the applicability of the Ornstein-Zernike correlation function, the half width at half maximum (HWHM) obtained in this procedure gives the inverse correlation length (ξ^{-1}) of the spatial correlations [45]. Figure 4(a) shows the critical behavior of the inverse correlation length measured at two satellite and the diffuse hexagon corner position. For the diffuse spots at two satellite positions, HWHM decreases to zero at T_P, in accordance with previous results [23]. The HWHM of the diffuse hexagon corner (A′ point) is almost temperature independent as it only slightly decreases when the temperature is lowered.

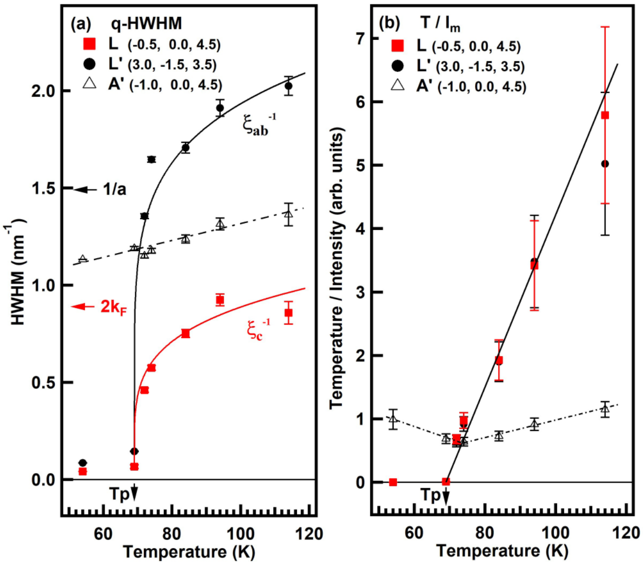

FIG. 4. (a) Momentum HWHM (in nm^{-1}) and (b) T/I$_m$ (temperature over intensity maximum) of diffuse spots at satellite positions L′ point (3, −1.5, 3.5) and L point (−0.5, 0, −4.5), scanned, respectively, in the $a^* + b^*$ and c^* directions. The HWHM and T/I$_m$ measured in the c^* direction at the position of a diffuse hexagon corner A′ point, (−1.0, 0, −4.5), are shown for comparison. T_P is for the temperature of the Peierls transition. $2k_F$ and $1/a$ indicate, respectively, the CDW modulation wave vector and the inverse minimal distance between two V in the (a, b) plane.

The generalized susceptibility at a satellite position is given by the intensity maximum of the diffuse scattering weighted by the temperature factor k_BT [46]. Its reciprocal value shows linear, Curie-Weiss, behavior [see Fig. 4(b)]. The generalized susceptibility measured at the A′ point is almost independent of temperature. There is just a broad and shallow dip at T_p.

B. Inelastic x-ray scattering

1. Phonon dispersion

Figure 5(a) shows the phonon dispersion measured by IXS. In the energy range 0–15 meV, there are two phonons bands: The low-energy phonon is indicated by red points, and the high-energy phonon by black triangles. The path followed along high-symmetry lines is indicated in Fig. 5(b). The phonon energy shows very small variations besides Γ-A, A-L, and A′-L lines. Note that in A′, the high-energy phonon has negligible intensity. Moreover, in A, the low-energy phonon has two components.

DFT calculations performed on the hexagonal and orthorhombic structure are presented in Fig. 6 of the Ref. [39].

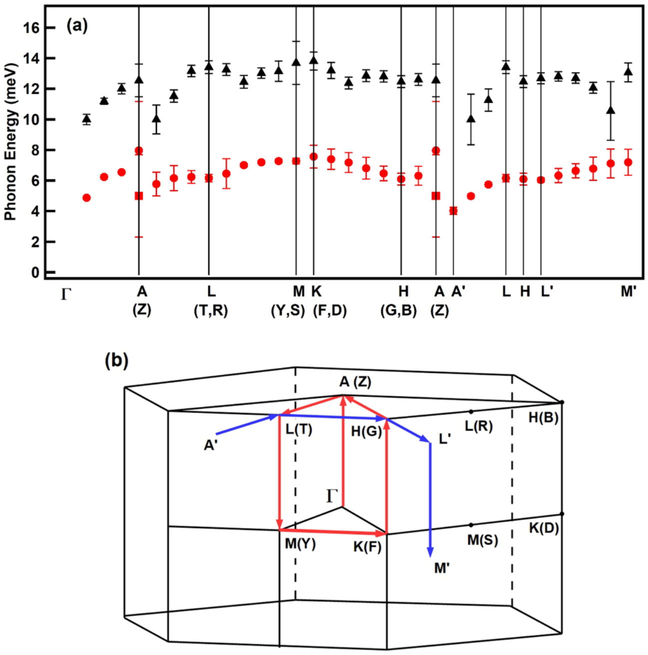

FIG. 5. (a) q dependence of the energy of the two phonons along high-symmetry lines, measured at 75 K. High-symmetry points are indicated for the hexagonal (orthorhombic) BZ. (b) The first BZ with the explored high-symmetry lines, Γ-A-L-M-K-H-A (red arrows). Additional path is explored out of the first BZ, A′-L-H-L′-M′ (blue arrows), where edges of diffuse hexagons appear. Note that the positions of the points Γ, M, K, M′ are not exact, but there is an error of 5% of the reduced wave vector in the $\boldsymbol{h}$ and $\boldsymbol{k}$ directions. Moreover, in the orthorhombic phase, at least 3 twins coexist. A general q point in experimental data becomes a superposition of nonequivalent points of the reciprocal orthorhombic unit cell. For example, the L point in the hexagonal phase becomes a superposition of T and R points in the orthorhombic phase.

The comparison with the calculations using the hexagonal structure is not useful here. The low-frequency phonon spectrum is strongly perturbed in the vicinity of the Γ point because of the instability leading to the hexagonal to orthorhombic transition. The calculations on the orthorhombic structure show that the phonons in the 0–15 meV energy range are essentially dispersionless besides when approaching the Γ point. In order to make the comparison easier, the corresponding points in the orthorhombic $\mathrm{Cmc}2_1$ space group, used in the DFT calculations, are given in parentheses in Fig. 5.

2. *Temperature evolution of the phonon energy*

Figures 6(a)–6(c) show IXS energy scans at different temperatures on L, L′, and A′ points, corresponding to the two satellites and the hexagon-diffuse corner [see Fig. 2(g) or Fig. 5(b)]. It clearly indicates that the phonon energy does not change with temperature. We can note that on cooling, the central peak (CP) intensity, mostly larger than the (LE, HE) phonon intensity, increases for L and L′, and decreases for the A′ point.

Temperature dependence of the energy position and the HWHM of the two phonon responses are given in Figs. 7(a) and 7(b). The energy of the two phonons at the two satellite positions does not decrease when the temperature approaches the MI transition: there is clearly no phonon softening. Moreover, the width of the low-energy phonon only slightly increases on approaching the MI transition.

From these data it is clear that there is no Kohn anomaly at the critical wave vector associated with the MI transition. The Peierls transition in $\mathrm{BaVS_3}$ is not phonon driven. Its character is not displacive, but of order-disorder type.

3. *Quasielastic scattering*

We are finally interested in the dynamics of the fluctuations which can be deduced from the profile of the IXS central peak measured at the position of a satellite. The central peak profile is analyzed by a Lorentzian function and deconvoluted by the experimental resolution of 2.65 meV (full width at half maximum). Its inverse HWHM measures the lifetime of the pretransitional fluctuations, while its integrated intensity divided by the temperature can be related to the generalized susceptibility. Figure 8(a) shows that the energy-HWHM of the central peak decreases almost linearly when approaching T_P. The lifetime of the pretransitional fluctuations thus diverges at T_P. At the same time, the inverse generalized susceptibility vanishes in a Curie-Weiss-like way, as shown in Fig. 8(b). Finally, note that the quasielastic scattering measured at the A′ point does not exhibit a critical behavior at T_P.

IV. DISCUSSION

Experimental results obtained by our DS and IXS investigations presented in Sec. III, show that $\mathrm{BaVS_3}$ exhibits inherent high-temperature disorder and a general lattice dynamics which are unusual for a Peierls system. Below we shall detail the uniqueness of these results in separated subsections.

A. The honeycomb-shaped DS

The first unexpected observation was an x-ray diffuse scattering pattern in form of hexagons in $l = n + 0.5c^*$ planes (n being an integer). It is clearly visible in the temperature range from T_P to at least 300 K, as shown in Fig. 2(b). Another pattern of diffuse spots, precursor to the Peierls transition, is detected above T_P [see Fig. 2(d)]. It will be discussed in the next section (Sec. IV B). The high-temperature hexagonal DS is thus due to some lattice disorder which is not directly related to the Peierls instability.

The numerical calculation of the honeycomb-shaped DS (see the Appendix) and the DFT calculations of the $\mathrm{BaVS_3}$ orthorhombic structure [39] show that it is mainly caused by an out of phase, c direction, low-frequency motion of the two Ba atoms in the unit cell. Such low-frequency phonon spectrum is corroborated by the IXS measurements (see Fig. 5), which will be discussed in Sec. IV C. However, the phonons are not the only contribution to the hexagon-shaped diffuse scattering. As shown in IXS scans at A′ point (diffuse hexagon corner) represented in Fig. 6(c), the (quasi-)elastic contribution is more important than the phonon intensity.

Although there is a relatively good agreement between the measured and calculated DS, there is certainly a more profound explanation for the presence of a so well-defined hexagonal shaped diffuse scattering pattern at high

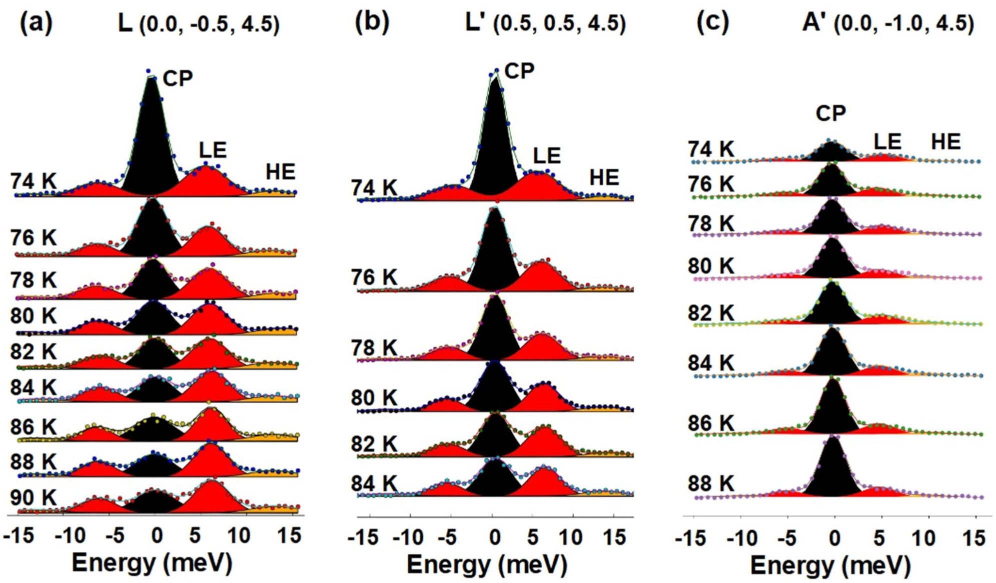

FIG. 6. IXS scans at two satellite positions, (a) L point at (0, −0.5, 4.5), (b) L′ point at (0.5, 0.5, 4.5), and (c) at the hexagon-diffuse corner, A′ point at (0, −1, 4,5). They are fitted with three structures: a central peak (CP, black), a low-energy phonon (LE, red) and a high-energy phonon (HE, yellow).

temperature in BaVS$_3$. Several other systems, with an underlying hexagonal symmetry, show such diffuse scattering [47]. For example, hexagonal shaped DS due to cluster short range order has been observed in binary metallic systems [48,49]. Another example are substituted perylene radical cation salts, whose local order can be modeled by a 2D hexagonal-like Ising system with frustrated interactions [50].

What can be the structural origin of the high-temperature Ba disorder in BaVS$_3$, giving rise to the hexagon-shaped DS? Note that the BaVS$_3$ structure is composed of succession of hexagonal packing of BaS$_3$ layers parallel to the (a, b) plane with V ions intercalated between them, as shown in Fig. 1. Observed Ba motion in (mainly) c direction corresponds to an out-of-plane shift from the BaS$_3$ layers. Reasons for such a shift can be the loss of cohesion in the hexagonal packing of these layers along c, some steric forces causing buckling of hexagonal layers, such as the poorly defined position of V atoms in their octahedral cavities, as proposed by recent

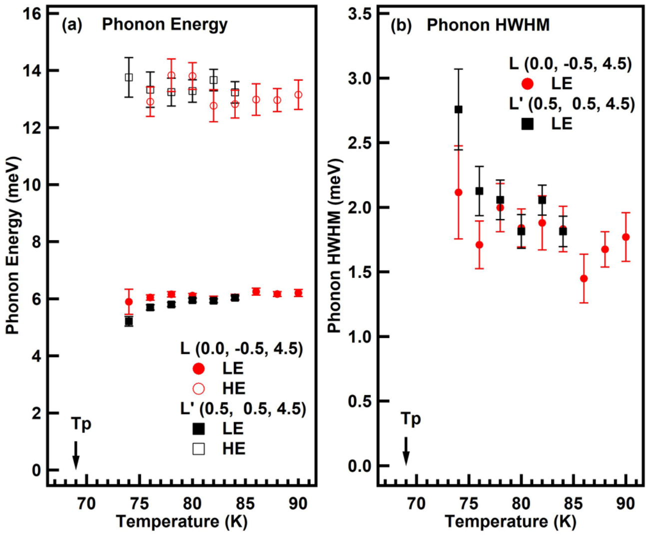

FIG. 7. Temperature evolution of the phonon (a) energy, (b) HWHM, measured at the two satellite positions. The error bars of the HWHM of the high-energy phonon being too large, the data are not shown.

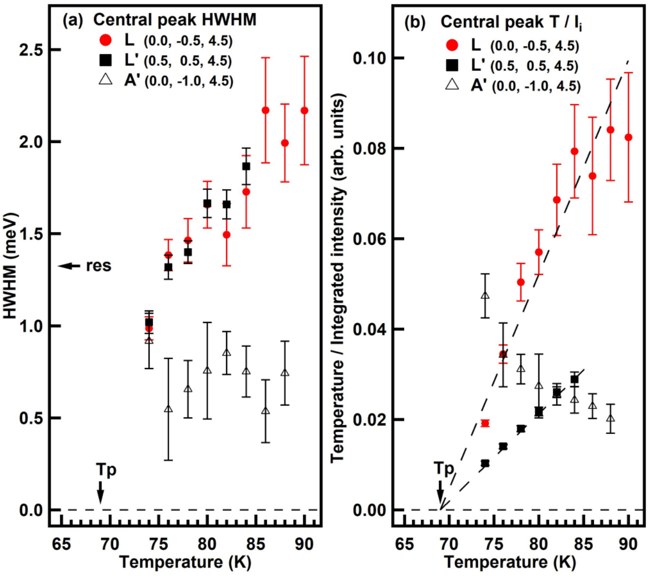

FIG. 8. IXS central pic (a) energy HWHM and (b) temperature over integrated intensity (T/I$_i$), measured at two satellite positions, L point at (0.0, −0.5, 4.5) (red circles), L′ point at (0.5, 0.5, 4.5) (black squares), and the position of the corner of a diffuse hexagon, A′ point at (0, −1, 4.5) (open black triangles). Horizontal arrow indicates the energy resolution of 1.325 meV (HWHM). The vertical arrow is for the temperature of the metal-insulator transition, as determined from the conductivity measurements. Dashed lines in (b) are guides for the eye. Data are extracted from the scans shown in Fig. 6.

structural refinements [16]. It is possible that such DS comes from frustrated interactions acting on Ba sites, resulting in local atomic displacements. This could explain the presence of a nondispersive, Einstein-type, lowest-energy phonon branches, which will be discussed in Sec. IV C.

It is not the low crystal quality, but the presence of this inherent dynamical disorder that can explain some properties of $BaVS_3$, in particular its relatively low conductivity, or "bad metallicity." Moreover, this peculiar DS, pointing to an inherent disorder, agrees with recent structural refinements [16]. They indicate that, contrary to earlier structural studies, $BaVS_3$ is in fact a 1D host- (V chain) guest (hcp BaS_3 matrix) composite system which lock-in to a common space group only below $T_m = 130$ K.

B. Anisotropy and critical diffuse scattering at the Peierls transition

The Peierls transition stabilizes a commensurate modulation with the main Fourier component being the critical wave vector corresponding to the L high-symmetry point of the hexagonal structure BZ. In the $l = n + 0.5c^*$ plane, the superstructure reflections are located either inside the above quoted diffuse hexagons (L point) or at their edge (L′ point), as shown in Fig. 2(e). Above T_P, the satellites transform into anisotropic diffuse spots [Fig. 2(d)] exhibiting a critical behavior when T_P is approached, as previously reported [23]. First, their peak intensity corrected for the thermal population factor has a Curie-Weiss behavior, $I_m/T \ \propto (T - T_P)^{-1}$, as T/I_m, plotted in Fig. 4(b), vanishes linearly when approaching T_P. Moreover, the HWHM of the diffuse spots (**q**-HWHM) in a chosen direction provides a measure of the inverse correlation length (ξ^{-1}) of the Peierls pretransitional fluctuations. This quantity has been measured along the c^* direction (ξ_c^{-1}) and $a^* + b^*$ direction (ξ_{ab}^{-1}). As the CDWs form in V-S chains, running in the c direction (equivalent to the c^* direction), ξ_c (ξ_{ab}) correspond to correlation lengths in the longitudinal (transverse) direction relatively to the CDW. Both ξ_c^{-1} and ξ_{ab}^{-1} vanish in a critical way at T_P as shown in Fig. 4(a). The temperature dependence of ξ_c^{-1}, agrees with the one previously reported in Ref. [23]. Figure 4(c) reports ξ_c^{-1} in the temperature range where it is always larger than the CDW modulation wavelength, ($\xi_c^{-1} \ < \ 2k_F$). Thus the data have been taken exclusively in the temperature range where the CDW fluctuations in the longitudinal direction are thermally coherent. For the ξ_{ab}^{-1}, at about 5 K above T_P it exceeds 1.48 nm^{-1}, which corresponds to $a = 0.675$ nm, the interchain V-V distance. Above this temperature CDW belonging to neighboring chains are not correlated, meaning that the system enters into a true 1D CDW fluctuation regime. Above 80 K, the temperature dependence of ξ_{ab}^{-1} deviates from the corresponding measurement in the previous work [23], as the two measurements have not been performed in exactly the same transverse directions.

Contrary to the diffuse scattering at L(L′) points, the **q**-HWHM and T/I_m temperature dependence measured at the A′ wave vector (diffuse hexagon corner) does not exhibit any critical behavior at T_P (see open triangles in Fig. 4). This confirms that the two types of DS detected in this study are not directly correlated. Finally, note that the diffuse lines detected until 170 K in the first x-ray diffuse scattering Laue diagrams of $BaVS_3$ [23] could correspond to sections of the reciprocal space in direction close to the diffuse hexagon edges, which are not directly related to the Peierls instability.

C. Einstein-type phonon modes

The low-energy phonon dispersion, measured by IXS at 75K (orthorhombic phase few K above T_P), is presented in Fig. 5. Two phonon branches, at 5–8 meV and 10–13 meV, can be clearly distinguished. The analysis presented in the Appendix shows that similar modes are found both at the reciprocal space positions of the diffuse hexagons (A′ and L′ points) and inside them (A, L, and H points). These two phonon branches exhibit a weak dispersion in the reciprocal space. The data are consistent with the calculated phonon spectrum of the orthorhombic phase [39]. The lower phonon branch corresponds to the calculated phonon bunch, at 7–9 meV, which is particularly dispersionless, with the exception of the region close to the Γ point, the region which is difficult to measure because of the presence of a Bragg reflection. The upper branch coincides with the lower part of the second phonon band, of more dispersive phonons in the 10- to 20-meV energy range. Low-frequency phonon modes of $BaVS_3$ can thus be described by a model of Einstein oscillators or localized atomic vibrations. This is a quite surprising result because the structure of $BaVS_3$ is derived from a compact packing where low-energy modes are expected to be much more dispersive. This implies the existence of weak interatomic coupling or of some competing elastic forces exerted by neighboring atoms. Such a feature can be related to the host-guest structure of $BaVS_3$ above $T_m = 130$ K.

D. Origin of the order-disorder Peierls dynamics

IXS energy scans at L and L′ positions of the critical wave vector of the Peierls transition of $BaVS_3$ are shown in Figs. 7(a) and 7(b). One recovers the two low-frequency phonon bands previously discussed. Our second unexpected observation is that the position of their maxima, at about 6 and 13 meV, respectively, does not change with temperature. Figure 7(c) summarizes the temperature dependence of the energy of the two phonons and reveals the absence of the Kohn anomaly in the phonon spectrum. There is thus no critical phonon energy softening when the Peierls transition is approached. This finding agrees with the phonon spectrum calculation in the orthorhombic phase [39] which does not reveal any negative phonon frequency.

Instead, there is a critical growth of a zero-energy response at L and L′ points, shown by the increase of the intensity of the CP, when approaching T_P, see Fig. 8(b). Indeed, its energy-integrated intensity I_i diverges at T_P in a Curie-Weiss way, as T/I_i vanishes linearly at the Peierls transition. This is, consequently, the same dependence as for T/I_m, derived from the intensity of the $2k_F$ Peierls pretransitional diffuse scattering at L and L′ points [see Fig. 4(b)]. In addition, the zero-energy response width progressively decreases when lowering the temperature. This shows that the nucleation of clusters happens with a mean lifetime τ which increases when approaching T_P. This corresponds to a diffusive dynamics with critical slowing down of cluster fluctuations.

The critical dynamics of $\mathrm{BaVS_3}$ is typical of order-disorder transition such as have been found in H-bond ferroelectrics [51]. In such phase transitions the low-temperature structure is achieved by the critical growth of quasistatic clusters, whose size is given by the correlation length ξ, while their lifetime τ is related to the inverse width of the zero-energy response. In this process the phase transition is attained by nucleation of domains of the low-temperature structure inside the high-temperature matrix. On a local scale, each atom is located in a double-well potential with the two minima indexed by an Ising variable (pseudospin). The local dynamics is controlled by a competition of the atomic thermal jump over the potential barrier and the interatomic coupling, described by coupled pseudospins [52]. This order-disorder transition exhibits a damped oscillator dynamics [51,52]. The finding of an order-disorder dynamics relying on the presence of local atomic displacements which form clusters is consistent with the observation of an Einstein-like phonon spectrum in $\mathrm{BaVS_3}$.

There are two classes of models which lead to an order-disorder type of the Peierls transition: the first class assumes a strong electron-phonon coupling (EPC) [15,53], while the second class assumes that the Peierls transition occurs in the nonadiabatic regime [9].

Models assuming a strong EPC are very similar. As proposed by Yu and Anderson [53], the strong EPC can result in a double-well potential via a polaronic capture mechanism between electrons and ions. In this model, applied to A15 superconductors, the local anharmonic potential is obtained via an interaction of electrons with a nondispersive optical mode (Einstein mode). The choice of an ion between the two minima of the potential at a particular site i is described by an Ising variable σ_i. The CDW state is achieved by the ordering of ions in a lattice of double-well sites. In this model there is similarity between the strong EPC limit of the Peierls instability and the Jahn-Teller effect. Similar features are obtained in strongly EPC chain models developed by Aubry and coworkers [14]. In the model of Gor'kov [15], applied to transition metal dichalcogenides, an arbitrary ionic movement is considered and different contributions to local elastic potentials are explicitly evaluated. Strong EPC results in trapping of the electron cloud in the vicinity of an ion i and the creation of a double-well potential. It leads to the Peierls energy gain and fixes the order of magnitude of the CDW gap. The intersite coupling between the σ_i's is described by the Ruderman-Kittel-Kasuya-Yosida interaction which oscillates with the $2k_F$ momentum between the pseudospins.

In both models assuming the strong EPC, a formation of distinct chemical bonds is expected on a local scale, which manifests itself by a sizable change of interatomic distances in the Peierls modulated phase. Across the MI transition of $\mathrm{BaVS_3}$, the amplitude of modulation of V-V bond distance is of the order of 0.1 Å [54], which is twice larger than the one (0.05 Å) in the case of the CDW of the blue bronze [9]. In the Peierls ground state of $\mathrm{BaVS_3}$, there is also a strong deformation of the sulfur octahedra surrounding each of the four nonequivalent V sites, resulting in a variation of V-S distances between different V sites which can be as large as 0.2 Å [16,54]. In addition, below T_P, the coordination of the V changes from 6 (V-$\mathrm{S_6}$ octahedron) to 5 (V-$\mathrm{S_5}$ square base pyramid) [16]. Such a feature could be also understood as the result of a collective Jahn-Teller instability.

The consequence of the strong variation of V-V and V-S distances induced by strong EPC is the modulation of transfer integrals and the modification of the occupancy of $\mathrm{A_{1g}}$ and $\mathrm{E_g}$ orbital states on V sites [33,54]. It could have a key role in the localization process of these orbitals. Even if the mechanism is different, it plays a role similar to the electron-electron coupling, inducing an interorbital $\mathrm{A_{1g}/E_g}$ charge transfer [31]. However, the strength of these interactions has not been clearly determined. Note that in the case of strong EPC the concepts of Fermi surface and of nesting are no longer relevant. However, the possibility of an interband nesting condition within $\mathrm{A_{1g}/E_{g1}}$ manifold has been deduced from angle-resolved photoemission measurements [55].

An order-disorder Peierls transition is also expected in the nonadiabatic limit in the case of extremely rapid phonon fluctuations compared to the lifetime time of the electron hole pairs (τ_{eh}), i.e., for a critical phonon frequency such that $\Omega_{2k_F} > 1/\tau_{eh}$ [9]. In that case the fluctuations of long living $2k_F$ electron-hole pairs cannot screen the interatomic interactions in order to form a Kohn anomaly. This situation has not yet be considered in the literature. However, the decrease of the Peierls transition of $\mathrm{BaVS_3}$ under pressure has been interpreted as due to a decrease of τ_{eh} due to a strengthening of the hybridization between the CDW-setting $\mathrm{A_{1g}}$ orbitals and the spin-carrying $\mathrm{E_{1g}}$ orbitals. Also the quantitative fit of T_P versus pressure leads to $1/\tau_{eh} \approx 4$ meV at ambiant pressure [37]. This leads to a central peak HWHM of 2.3 meV (= 4/7 τ_{eh}, according to Ref. [9]) which agrees with the high temperature measurements of Fig. 8(a).

We have considered two possible mechanisms of Peierls transition which could account for the order-disorder type of dynamics for the Peierls transition of $\mathrm{BaVS_3}$. Either the Peierls transition occurs in the strong EPC limit or in the nonadiabatic limit. The two mechanisms are not exclusive. It is interesting to remark that in the literature theories involving a strong EPC do not consider the effect of nonadiabaticity. On the other hand, nonadiabatic processes do not necessarily require a strong EPC. Thus at the present stage of our investigation it is difficult to state which mechanism is appropriated for $\mathrm{BaVS_3}$.

E. Comparison with other Peierls-like systems

Among the Peierls systems the finding of an order-disorder Peierls dynamics in $\mathrm{BaVS_3}$ is unique. Another candidate is possibly $\mathrm{VO_2}$, another nonstandard Peierls system [56]. In more standard 1D Peierls systems such as the Krogmann salt, $\mathrm{K_2Pt(CN)_4Br_{0.3}\cdot 3H_2O}$ [6], and the blue bronze $\mathrm{K_{0.3}MoO_3}$ [7], a pronounced $2k_F$ Kohn anomaly is observed above T_P. The same is in the 2D CDW metals 2H-$\mathrm{NbSe_2}$ [12] and the tellurides $\mathrm{DyTe_3}$, $\mathrm{TbTe_3}$ [57], and $\mathrm{ZrTe_3}$ [58]. A confusing situation occurs for 1D transition metal trichalcogenides where the Kohn anomaly was not detected. From this nondetection, it has been argued that the Peierls transition of $\mathrm{NbSe_3}$ occurs in the strong EPC limit [59]. However, recent phonon spectrum

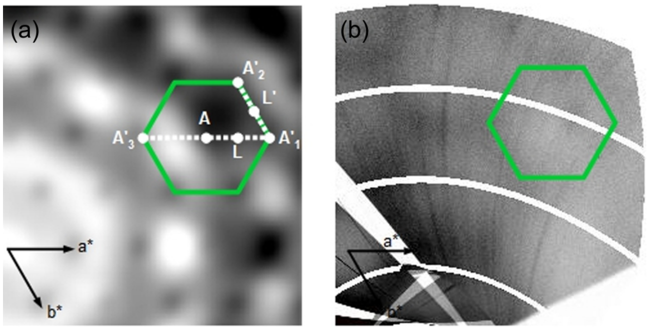

FIG. 9. (a) Calculated TDS intensity in the (*h*, *k*, 3.5) plane, corresponding to the Cmc2_1 space group, indexed in hexagonal settings. The green hexagon, white dotted lines and particular points A'_1, L′, A'_2, A, indicate the portion of the momentum space where the phonon analysis was performed. (b) Reconstruction of the measured (*h*, *k*, 3.5) plane at 114 K. The green hexagon indicates the same region as in (a).

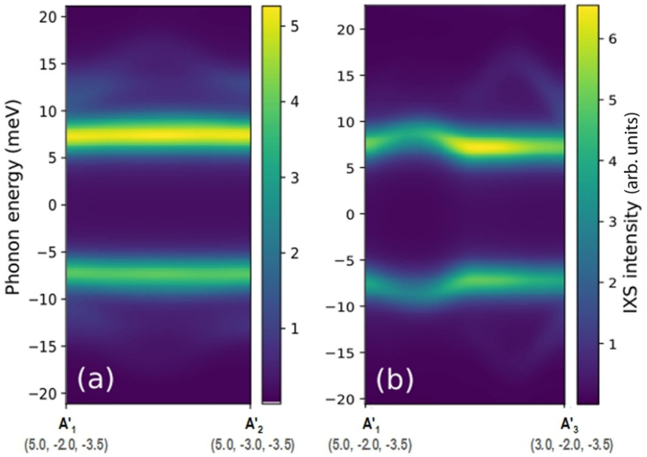

FIG. 10. Dispersion of low-energy phonons along $A'_1 \rightarrow A'_2$ (a) and $A'_1 \rightarrow A'_3$ (b) directions in reciprocal space.

calculation predict the existence of a giant Kohn anomaly in TaS_3 with a negative frequency at $2k_F$ momentum [60].

On the other hand, in many systems where the spin-Peierls instability occurs, the transition takes place in the nonadiabatic limit [9,61,62]. In such systems, an order-disorder critical spin-Peierls dynamics is predicted [63–65] and observed in inorganic $CuGeO_3$ [66] and organic $(TMTTF)_2PF_6$ [67] spin-Peierls compounds.

V. CONCLUSION

Our TDS and IXS measurements show that the Peierls transition in $BaVS_3$ is an order-disorder transition with damped oscillator dynamics. The two possible models explaining this type of Peierls instability include either a strong electron-phonon coupling or a nonadiabaticity, the two mechanisms being nonexclusive. At the present state of our study it is difficult to state which mechanism is appropriated for $BaVS_3$.

ACKNOWLEDGMENT

The help of Aleksandra Chumakova during the experiment as well as continuous discussion with Lázsló Forró and Alla Arakcheeva, particularly concerning recent structural results, are gratefully acknowledged.

APPENDIX

The phonon mode analysis is performed in the $l = 3.5$ plane along the white dotted lines in Fig. 9(a):

(i) $A'_1 \rightarrow A'_2$ [(5, −2, 3.5) → (5, −3, 3.5)], corresponding to a diffuse hexagon edge.

(ii) $A'_1 \rightarrow A'_3$ [(5, −2, 3.5) → (3, −2, 3.5)], crossing a hexagon center.

The first/second scan crosses reciprocal space positions L′/L, respectively, where satellites appear below T_P.

The equivalent portion of the reciprocal space in the reconstructed $l = 3.5$ plane is shown in Fig. 9(b).

Figures 10(a) and 10(b) shows the dispersion of low-energy phonons in the two scanned directions. In the $A'_1 \rightarrow A'_2$ direction, the phonons are dispersionless [see Fig. 10(a)], while along $A'_1 \rightarrow A'_3$, a small energy variation is observed close to the L point [Fig. 10(b)].

Table I shows phonon energy and TDS intensity depicted in selected points of the reciprocal space, along A'_1-A'_2 and A'_1-A'_3 directions. Low-energy phonons of about 7–9 meV strongly participate to the TDS intensity.

Table II gives normal coordinates of six lowest phonon modes. Important components are underlined by bold characters. It shows clearly a prominent Ba-motion, the contribution of S and particularly V being at least 5–10 times smaller. Modes 1 and 3 are mostly an out-of-phase movement of the two Ba atoms in the unit cell. The first, which has particularly important contribution to the TDS intensity, concerns mostly a *z*-axis movement, even if the the *y*-axis motion is not negligible. Modes 2/4/6 are, respectively, important *x*-axis-out-of-phase/*y*-axis-in-phase/*z*-axis-in-phase motions of Ba atoms.

Finally, for the sake of comparison with the Figs. 2(b)–2(e), the reconstructions of the (*h*, *k*, 3.5) plane at 300 K, 114 K,

TABLE I. Calculated energy (*E* in meV) and TDS intensity (*I* in arb. units) of the first 10 phonon modes, as classified by their energy. The analysis is performed in four points in the (*h*, *k*, 3.5) plane, which are indicated in Fig. 9(a). Six of them belong to the lowest-energy phonon band, which contributes strongly to the TDS intensity, as highlighted in bold.

(*h*, *k*)	A'_1	(5,-2)	L′	(5,−2.5)	A'_2	(5,−3)	A	(4,−2)
Mode	*E*	*I*	*E*	*I*	*E*	*I*	*E*	*I*
1	6,95	0,77	7,11	**9,56**	6,95	**6,28**	6,95	**4,96**
2	6,95	**10,35**	7,11	1,68	6,95	1,93	6,95	**6,42**
3	7,06	2,12	7,46	1,49	7,06	0,81	7,06	1,65
4	7,06	0,57	7,46	**6,01**	7,06	1,43	7,06	2,10
5	7,78	**6,35**	8,81	2,51	7,78	0,79	7,78	**3,28**
6	7,78	1,04	8,81	1,82	7,78	**10,11**	7,78	**8,24**
7	11,09	0,45	12,95	0,60	11,09	0,37	11,09	0,01
8	11,09	2,49	12,95	0,87	11,09	0,05	11,09	0,01
9	12,89	0,32	15,83	0,74	12,89	2,95	12,89	0,33
10	12,89	1,57	15,83	0,09	12,89	0,52	12,89	0,51

TABLE II. Six lowest-energy-mode normal coordinates.

At.	Atom		Mode 1			Mode 2			Mode 3	
nb.	type	*x*	*y*	*z*	*x*	*y*	*z*	*x*	*y*	*z*
1	S	−0.018638	0.045221	0.005759	0.001864	−0.000473	−0.012033	−0.017230	0.071573	0.031629
2	S	0.012955	0.006649	0.010771	0.035247	−0.025505	0.020174	0.034880	−0.099225	0.000762
3	S	−0.011107	0.008052	0.010000	0.028942	0.015266	−0.015181	−0.035594	−0.100014	0.000770
4	S	0.019254	0.045498	0.006630	−0.001752	−0.004019	0.016281	0.016890	0.071239	0.031032
5	S	0.000240	0.035703	−0.033482	−0.011860	−0.001400	−0.000408	−0.000199	0.048889	−0.049679
6	S	0.001243	0.007513	0.018790	0.044826	−0.002350	−0.001278	−0.000820	−0.031234	0.011595
7	V	−0.000209	0.007619	−0.035802	−0.006179	−0.000126	0.001224	0.000015	0.006375	0.006592
8	V	0.000012	−0.015077	−0.003328	−0.000416	0.000901	0.000083	−0.000004	0.004271	−0.000796
9	Ba	−0.006414	**0.252127**	**−0.670397**	**−0.161270**	0.001964	0.032208	−0.000365	**0.572453**	**0.149188**
10	Ba	0.006997	**−0.131141**	**0.670494**	**0.169363**	−0.003925	−0.026332	−0.000107	**−0.732379**	**−0.237025**
At.	Atom		Mode 4			Mode 5			Mode 6	
nb.	type	*x*	*y*	*z*	*x*	*y*	*z*	*x*	*y*	*z*
1	S	0.025130	−0.063164	−0.004178	−0.021247	0.015127	0.009098	−0.002786	0.033906	0.000852
2	S	0.019749	−0.060383	0.027532	0.006365	0.000293	0.007071	0.010326	−0.010352	0.007651
3	S	−0.019977	−0.059950	0.027062	0.003714	−0.003397	−0.008965	−0.009612	−0.009688	0.007838
4	S	−0.025640	−0.063808	−0.003476	−0.016370	−0.010477	−0.004794	0.003838	0.035239	0.001556
5	S	−0.000040	−0.014336	−0.011538	−0.021412	0.001843	−0.001384	0.000770	0.010397	0.006744
6	S	0.000576	−0.043381	−0.043496	0.015734	−0.001214	0.000535	0.000649	−0.007179	0.004498
7	V	0.000001	0.003980	−0.008552	−0.000598	0.000416	−0.001099	−0.000016	0.014587	0.000744
8	V	−0.000103	0.006367	0.004775	0.002839	−0.000308	−0.000288	0.000080	0.005872	0.041715
9	Ba	0.006294	**−0.588395**	**−0.129169**	−0.053814	−0.019800	−0.016180	−0.000322	−0.005712	**−0.708018**
10	Ba	0.000950	**−0.570885**	0.059024	−0.044477	−0.005120	0.015988	−0.000659	0.086928	**−0.695822**

74 K, and 69 K, presented in the same intensity range, are shown Fig. 11. It shows that the honeycomb-shaped diffusion is hardly visible at low temperature if the intensity is not magnified.

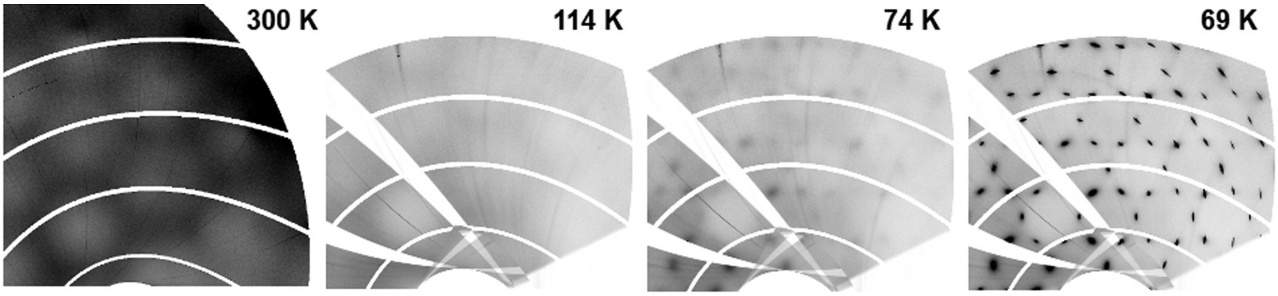

FIG. 11. Reconstruction of the (h, k, 3.5) plane at 300 K, 114 K, 74 K, and 69 K, presented in the same intensity range.

[1] W. Kohn, Phys. Rev. Lett. **2**, 393 (1959).

[2] E. J. Woll and W. Kohn, Phys. Rev. **126**, 1693 (1962).

[3] F. Giustino, Rev. Mod. Phys. **89**, 015003 (2017).

[4] A. M. Afana'sev and Yu. Kagan, Zh. Eksp. Teor. Fiz. **43**, 1456 (1962) [Soviet Phys. JETP **16**, 1030 (1963)].

[5] M. J. Rice and S. Strässler, Solid State Commun. **13**, 125 (1973).

[6] B. Renker, H. Rietschel, L. Pintschovius, W. Gläser, P. Brüesch, D. Kuse, and M. J. Rice, Phys. Rev. Lett. **30**, 1144 (1973).

[7] J. P. Pouget, B. Hennion, C. Escribe-Filippini, and M. Sato, Phys. Rev. B **43**, 8421 (1991).

[8] B. Guster, M. Pruneda, P. Ordejón, E. Canadell, and J.-P. Pouget, Phys. Rev. Mater. **3**, 055001 (2019).

[9] J.-P. Pouget, C. R. Phys. **17**, 332 (2016).

[10] G. Shirane, S. M. Shapiro, R. Comès, A. F. Garito, and A. J. Heeger, Phys. Rev. B **14**, 2325 (1976).

[11] D. E. Moncton, J. D. Axe, and F. J. DiSalvo, Phys. Rev. B **16**, 801 (1977).

[12] F. Weber, S. Rosenkranz, J.-P. Castellan, R. Osborn, R. Hott, R. Heid, K.-P. Bohnen, T. Egami, A. H. Said, and D. Reznik, Phys. Rev. Lett. **107**, 107403 (2011).

[13] C. M. Varma and A. L. Simons, Phys. Rev. Lett. **51**, 138 (1983).

[14] P. Y. Le Daeron and S. Aubry, J. Phys. Colloq. **44**, C3-1573 (1983).

[15] L. P. Gor'kov, Phys. Rev. B **85**, 165142 (2012).

[16] A. Arakcheeva, P. Pattinson, G. Chapuis, H. Berger, N. Barišić, and L. Forró, Acta Cryst. B (unpublished).

[17] R. A. Gardner, M. Vlasse, and A. Wold, Acta Crystallogr. B **25**, 781 (1969).

[18] G. Mihály, I. Kézsmárki, F. Zámborszky, M. Miljak, K. Penc, P. Fazekas, H. Berger, and L. Forró, Phys. Rev. B **61**, R7831(R) (2000).

[19] F. Sayetat, M. Ghedira, M. Marezio, and J. Chenavas, J. Phys. C: Solid State Phys. **15**, 1627 (1982).

[20] N. Barisic, Ph.D. thesis, Ecole Polytechnique Fédérale de Lausanne, 2004.

[21] V. Ilakovac, N. B. Brookes, J. Criginski Cezar, P. Thakur, V. Bisogni, C. Dallera, G. Ghiringhelli, L. Braicovich, S. Bernu, H. Berger, L. Forró, A. Akrap, and C. F. Hague, J. Phys: Condens. Matter **24**, 045503 (2012).

[22] T. Inami, K. Ohwada, H. Kimura, M. Watanabe, Y. Noda, H. Nakamura, T. Yamasaki, M. Shiga, N. Ikeda, and Y. Murakami, Phys. Rev. B **66**, 073108 (2002).

[23] S. Fagot, P. Foury-Leylekian, S. Ravy, J.-P. Pouget, and H. Berger, Phys. Rev. Lett. **90**, 196401 (2003).

[24] H. Nakamura, T. Yamasaki, S. Giri, H. Imai, M. Shiga, K. Kojima, M. Nishi, K. Kakurai, and N. Metoki, J. Phys. Soc. Jpn. **69**, 2763 (2000).

[25] P. Leininger, V. Ilakovac, Y. Joly, E. Schierle, E. Weschke, O. Bunau, H. Berger, J.-P. Pouget, and P. Foury-Leylekian, Phys. Rev. Lett. **106**, 167203 (2011).

[26] R. A. de Souza, U. Staub, V. Scagnoli, M. Garganourakis, Y. Bodenthin, and H. Berger, Phys. Rev. B **84**, 014409 (2011).

[27] P. Foury-Leylekian, P. Leininger, V. Ilakovac, Y. Joly, S. Bernu, S. Fagot, and J. Pouget, Physica B **407**, 1692 (2012).

[28] M. Nakamura, A. Sekiyama, H. Namatame, A. Fujimori, H. Yoshihara, T. Ohtani, A. Misu, and M. Takano, Phys. Rev. B **49**, 16191 (1994).

[29] L. Mattheiss, Solid State Commun. **93**, 791 (1995).

[30] M.-H. Whangbo, H.-J. Koo, D. Dai, and A. Villesuzanne, J. Solid State Chem. **165**, 345 (2002).

[31] F. Lechermann, S. Biermann, and A. Georges, Phys. Rev. Lett. **94**, 166402 (2005).

[32] F. Lechermann, A. Georges, A. Poteryaev, S. Biermann, M. Posternak, A. Yamasaki, and O. K. Andersen, Phys. Rev. B **74**, 125120 (2006).

[33] F. Lechermann, S. Biermann, and A. Georges, Phys. Rev. B **76**, 085101 (2007).

[34] S. Fagot, P. Foury-Leylekian, S. Ravy, J.-P. Pouget, É. Lorenzo, Y. Joly, M. Greenblatt, M. V. Lobanov, and G. Popov, Phys. Rev. B **73**, 033102 (2006).

[35] T. Ivek, T. Vuletić, and S. Tomić, A. Akrap, H. Berger, and L. Forró, Phys. Rev. B **78**, 035110 (2008).

[36] L. Forró, R. Gaál, H. Berger, P. Fazekas, K. Penc, I. Kézsmárki, and G. Mihály, Phys. Rev. Lett. **85**, 1938 (2000).

[37] S. Bernu, P. Fertey, J.-P. Itié, H. Berger, P. Foury-Leylekian, and J.-P. Pouget, Phys. Rev. B **86**, 235105 (2012).

[38] J. Sugiyama, D. Andreica, O. K. Forslund, E. Nocerino, N. Matsubara, Y. Sassa, Z. Guguchia, R. Khasanov, F. L. Pratt, H. Nakamura, and M. Månsson, Phys. Rev. B **101**, 174403 (2020).

[39] A. Girard, V. Ilakovac, M. Stekiel, W. Morgenroth, H. Berger, T. Yoshikazu, T. Hasegawa, A. Bosak, and B. Winkler, Phys. Rev. B **99**, 144104 (2019).

[40] H. Kuriyaki, H. Berger, S. Nishioka, H. Kawakami, K. Hirakawa, and F. Lévy, Synth. Met. **71**, 2049 (1995).

[41] A. Girard, T. Nguyen-Thanh, S. M. Souliou, M. Stekiel, W. Morgenroth, L. Paolasini, A. Minelli, D. Gambetti, B. Winkler, and A. Bosak, J. Synchr. Radiat. **26**, 272 (2019).

[42] S. J. Clark, M. D. Segall, C. J. Pickard, P. J. Hasnip, M. I. J. Probert, K. Refson, and M. C. Payne, Z. Kristallogr. **220**, 567 (2005).

[43] K. Refson, P. R. Tulip, and S. J. Clark, Phys. Rev. B **73**, 155114 (2006).

[44] A. Bosak, D. Chernyshov, B. Wehinger, B. Winkler, M. Le Tacon, and M. Krisch, J. Phys. D: Appl. Phys. **48**, 504003 (2015).

[45] R. Moret and J. P. Pouget, Structural studies of phase transitions in one-dimensional conductors, in *Chrystal Chemistry and Properties of Materials with Quasi-One-Dimentional Structures*, edited by J. Rouxel (D. Riedel, Dordrecht, 1986), pp. 87–134.

[46] The q-dependent diffuse scattering $I(q)$ is proportional to the q Fourier component of the displacement-displacement correlation function $\langle |u_q|^2 \rangle$ which is related in the classical limit to the generalized susceptibility $\chi(q)$ by the expression $\langle |u_q|^2 \rangle = k_B T \chi(q)$ [45]. In the Ornstein approximation $\chi(q)$ has a Lorentzian shape whose HWHM defines ξ^{-1}.

[47] T. R. Welberry and R. L. Withers, J. Appl. Cryst **20**, 280 (1987).

[48] R. Moret, M. Huber, and R. Comès, Phys. Stat. Sol. **88**, 695 (1976); J. Phys. Colloq. **38**, C7-202 (1977).

[49] R. De Ridder, G. Van Tendeloo, D. Van Dyck, and S. Amelinkcx, J. Phys. Colloq. **38**, C7-178 (1977).

[50] V. Ilakovac, S. Ravy, A. Moradpour, L. Firlej, and P. Bernier, Phys. Rev. B **52**, 4108 (1995).

[51] R. Blinc and B. Žekš, Adv. Phys. **21**, 693 (1972).

[52] P. G. De Gennes, Sol. State Commun. **1**, 132 (1963).

[53] C. C. Yu and P. W. Anderson, Phys. Rev. B **29**, 6165 (1984).

[54] S. Fagot, P. Foury-Leylekian, S. Ravy, J. P. Pouget, M. Anne, G. Popov, M. V. Lobanov, and M. Greenblatt, Solid State Sci. **7**, 718 (2005).

[55] S. Mitrovic, P. Fazekas, C. Søndergaard, D. Ariosa, N. Barišić, H. Berger, D. Cloëtta, L. Forró, H. Höchst, I. Kupčić, D. Pavuna, and G. Margaritondo, Phys. Rev. B **75**, 153103 (2007).

[56] J.-P. Pouget, Basic aspects of the metal-insulator transition of the vanadium dioxide, VO_2: A critical review (unpublished).

[57] M. Maschek, D. A. Zocco, S. Rosenkranz, R. Heid, A. H. Said, A. Alatas, P. Walmsley, I. R. Fisher, and F. Weber, Phys. Rev. B **98**, 094304 (2018).

[58] M. Hoesch, A. Bosak, D. Chernyshov, H. Berger, and M. Krisch, Phys. Rev. Lett. **102**, 086402 (2009).

[59] H. Requardt, J. E. Lorenzo, P. Monceau, R. Currat, and M. Krisch, Phys. Rev. B **66**, 214303 (2002).

[60] B. Guster, M. Pruneda, P. Ordejón, E. Canadell, and J.-P. Pouget, arXiv:2012.06812v2 [cond-mat.mtrl-sci] (2020).

[61] R. Citro, E. Orignac, and T. Giamarchi, Phys. Rev. B **72**, 024434 (2005).

[62] J. P. Pouget, Physica B **407**, 1762 (2012).

[63] C. Gros and R. Werner, Phys. Rev. B **58**, R14677 (1998).

[64] J. P. Pouget, Eur. Phys. J. B **20**, 321 (2001).

[65] J. P. Pouget, Eur. Phys. J. B **24**, 415 (2001).

[66] M. Braden, B. Hennion, W. Reichardt, G. Dhalenne, and A. Revcolevschi, Phys. Rev. Lett. **80**, 3634 (1998).

[67] J. P. Pouget, P. Foury-Leylekian, S. Petit, B. Hennion, C. Coulon, and C. Bourbonnais, Phys. Rev. B **96**, 035127 (2017).